

Waves in Random and Complex Media

ISSN: (Print) (Online) Journal homepage: <https://www.tandfonline.com/loi/twrm20>

Electrical magneto hydrodynamic Jeffrey fluid flow with thermal radiation through stretched cylinder

Kotha Gangadhar, M. Prameela, Konduru Bhanu Lakshmi & Ali J. Chamkha

To cite this article: Kotha Gangadhar, M. Prameela, Konduru Bhanu Lakshmi & Ali J. Chamkha (2022): Electrical magneto hydrodynamic Jeffrey fluid flow with thermal radiation through stretched cylinder, *Waves in Random and Complex Media*, DOI: [10.1080/17455030.2022.2099598](https://doi.org/10.1080/17455030.2022.2099598)

To link to this article: <https://doi.org/10.1080/17455030.2022.2099598>



Published online: 17 Jul 2022.



Submit your article to this journal [↗](#)



Article views: 78



View related articles [↗](#)



View Crossmark data [↗](#)



Electrical magneto hydrodynamic Jeffrey fluid flow with thermal radiation through stretched cylinder

Kotha Gangadhar^a, M. Prameela^b, Konduru Bhanu Lakshmi^c and Ali J. Chamkha^d

^aDepartment of Mathematics, AcharyaNagarjuna University Campus, Ongole, Andhra Pradesh, India;

^bDepartment of Mathematics, Prasad V. Potluri Siddharth Institute of Technology, Vijayawada, Andhra Pradesh, India;

^cDepartment of Mathematics, Lakireddy Bali Reddy College of Engineering, Mylavaram, Andhra Pradesh, India;

^dFaculty of Engineering, Kuwait College of Science and Technology, Doha District, Kuwait

ABSTRACT

The current study investigates the effects of electrical and magnetic fields on the stagnation point in Jeffrey fluid flow along a stretched cylinder with thermal radiation and chemical reaction. The Cattaneo-Christov model with double stratification and thermal relaxation was used. Heat and mass transfer are investigated. Governing partial differential equations are converted to ordinary differential equations using similarity transformation. FEM technique is used to calculate the numerical solution of a set of nonlinear coupled equations with coding implementation in MATLAB. The numerical outcomes of current work are more significant when they are correlated with previous work. The interest in computational attempts at the formation of boundary layers for concentration distribution, fluid velocity, and temperature increases as significant parameters are varied. The main outcomes of this study are that increasing electrical effects is to decrease fluid velocity while increasing magnetic parameters is to decrease the flow velocity. Another effect is that an increase in thermal radiation and heat transfer raises the temperature of the fluid. Furthermore, the fluid concentration is reduced due to the increased level of a chemical reaction.

ARTICLE HISTORY

Received 19 March 2022

Accepted 4 July 2022

KEYWORDS

FEM; Jeffrey fluid; electric field; heat source; double stratification

Nomenclature

$(\tilde{u}_1, \tilde{v}_1)$	Velocity components (ms^{-1})
$(\tilde{x}_1, \tilde{r}_1)$	Cylindrical coordinates (m)
\tilde{u}_w	Stretching velocity (ms^{-1})
U_∞	Free stream velocity (ms^{-1})
U_0	Reference velocity (ms^{-1})
b	Radius of the cylinder
s	Characteristic length
T	Fluid temperature (K)
T_w	Surface temperature (K)

CONTACT Ali J. Chamkha  a.chamkha@kcst.edu.kw

T_{∞}	Ambient temperature (K)
T_0	Reference temperature (K)
$\rho_1 C_p$	Specific heat ($Jkg^{-1}K^{-1}$)
C	Fluid concentration
C_w	Concentration at surface
C_{∞}	Ambient concentration
C_0	Reference concentration
D	Brownian diffusion ($kgm^{-1}s^{-1}$)
k	Thermal conductivity ($Wm^{-1}K^{-1}$)
k^*	Mean absorption coefficient ($1m^{-1}$)
E_0	Electric field strength (NC^{-1})
B_0	Magnetic field strength ($NsC^{-1}m^{-1}$)
q_{rad}	Radiative heat flux (Wm^{-2})
Rd	Radiation parameter
Pr	Prandtl number
Nu	Local Nusselt number
Sh	Local Sherwood number
Sc	Schmidt number
C_p	Heat capacity ($Jkg^{-1}K^{-1}$)
E	Electric parameter
M	Magnetic parameter
S	Thermal stratified variable
A	Moments ratio

Greek symbols

ρ_1	Density (kgm^{-3})
σ_1	Electrical conductivity (Sm^{-1})
μ	Kinetic viscosity (m^2s^{-1})
λ_1	Fluid relaxation time
λ_2	Fluid retardation time
λ_3	Thermal relaxation parameter for temperature
λ_4	Thermal relaxation parameter for mass flux
δ	Heat source factor
δ_1	Chemical reaction variable
β	Deborah number
η	Similarity variable
γ	Thermal relaxation parameter
γ_1	Concentration relaxation factor
θ_1	Dimensionless temperature
ϕ_1	Dimensionless concentration
σ^*	Stefan–Boltzman constant ($Wm^{-2}K^{-4}$)

Subscripts

w	Condition at wall
∞	Condition in free stream

1. Introduction

In comparison to Newtonian fluids, non-Newtonian fluids play an important role in manufacturing and technological fields. In everyday life, we have seen more applications on non-Newtonian fluids such as ketchup, toothpaste, paint, blood, and so on. There is no relationship between stress rate and strain in non-Newtonian fluids. Non-Newtonian fluids play an important role in engineering. The Navier–Stokes model is inapplicable for estimating the behavior of such fluids. In general, the mathematical formulation for this type of fluid is complex. Non-Newtonian fluids were encountered in petroleum, geophysics, and chemical processes. Nonlinear fluids are indicated by some oils, ketchup, foams, lubricants, soaps, and other substances. Jeffrey fluid plays a significant role in the relaxation and retardation time explanation. Hussain et al. [1] explained the consequences of heat source, thermal relaxation and double stratification in the Jeffrey liquid stream. Ijaz Khan and Alzahrani [2] used the shooting technique to solve heat transport in the Jeffrey fluid along a stretched curved surface with the existence of entropy minimization and activation energy. Jeffrey fluid flow in a porous microchannel with linear reabsorption on axisymmetric flow was analyzed by Mehboob et al. They discovered that increasing the relaxation time reduces the axisymmetric flow. Bhatti et al. [3] investigated the effects of chemically reactive mass transfer on the non-Newtonian type in the presence of a magnetic effect. Peshkov et al. [4] investigated the behavior of nonlinear viscoelastic flows using a first-order hyperbolic model. The impact of inclined thermal radiation and magnetic field on non-Newtonian blood flow conveying hybrid magnetic nanoparticles was scrutinized by Ketchate et al. [5]. Selimefendigil and Oztop [6] described the different cooling systems. Loenko et al. [7] investigated the unsteady natural convection of a nonlinear liquid with a sinusoidal wall temperature. Nadeem et al. [8] defined the peristaltic flow of a heated Jeffrey fluid inside an elliptic cross-sectional duct. Oke [9] calculated numerical results for modified Eyring Powell fluid flow over a linearly stretching flat plate. They discovered that increasing the velocity resulted in a lower heat transfer rate.

Engineering and manufacturing demand exists for a steady point of stagnation in a flow field. It is also used in ground liquid flow, among other things. Mahapatra and Gupta [10] investigated the flow of a Stagnation point across a stretching sheet. Pop et al. [11] investigated the effect of radiation on flow near a stagnation point. Mandal et al. [12] investigated the effects of magnetic body force and radiative heat transport on mixed convective stagnation point slip flow of nano liquid. Iqbal et al. [13] have considered the composite effects of homogeneous–heterogeneous reactions on magnetic forced convection flow in a viscoelastic fluid near a stagnation point. Gangadhar et al. [14] studied nodal or saddle stagnation point slip flow for convectional hybrid nanofluid flow. Shafiq et al. [15] studied the effect of ‘Double stratification flow of stagnation point Walter’s B nano- fluid flow via Riga plate’. Chu et al. [16] studied the 3D steady and incompressible laminar Homann stagnation point nano liquid flow over a porous moving surface. Zhao et al. [17] investigated theoretically the entropy generation with heat and mass transport in mixed hydro dynamics stagnation point flow across the stretchable sheet. Nguyen et al. [18] obtained the finite element simulation for the mixed convective flow owing to a slanted stagnation point along a vertically moving plane. Khan et al. [19] considered the unsteady water-based hybrid nano liquid over a radially permeable shrinking or stretching surface.

Radiation impact has piqued the interest of many scientists due to its numerous applications in engineering fields. For example, in high-temperature spacecraft operations, such as rockets, the main source of heat transfer via electromagnetic waves is radiation. Khan et al. [20] investigated the chemical reaction and nonlinear radiation impacts during unsteady motion. Luo et al. [21] investigate the effective thermal conductivity of porous materials in the presence of thermal radiation. Liu et al. [22] investigated the effect of porosity and fiber volume fraction on the useful thermal conductivity of composite materials. Raza et al. [23] investigated the two-dimensional MHD flow of a micropolar fluid in a porous medium using thermal radiation. Mumraiz et al. [24] studied the generation of entropy in electrical MHD hybrid nanofluid with non-uniform heat flux. Suganya et al. [25] probe the unsteady boundary layer flow of rotating hybrid nanoparticles on a stretched moving surface in the presence of activation energy. Mahabaleshwar et al. [26] explored the numerical experiment for nonlinear fluid flow due to a porous shrinking/stretching sheet with heat transfer. Ali et al. [27] investigated the 'Stefan blowing and thermal radiation on nanofluid flow containing microorganisms with ablation or accretion of leading edge' using the FEM approach. 'The mixed convection stagnation point's flow and heat transfer in an incompressible Cross fluid over a permeable shrinking sheet with suction and radiation' is investigated by Jamaludin et al. [28]. Acharya [29] worked on the thermal control of radiative natural convection hybrid nanofluid flow inside a square field. An exact analytical solution of a hybrid nanofluid flow over a stretching/shrinking sheet in the presence of thermal radiation and mass transpiration was scrutinized by Mahabaleshwar et al. [30]. Gangadhar et al. [31] investigated the thermal radiative impact on couple stress fluid.

Cattaneo revised by including a thermal relaxation time factor. Christov also changes the time factor by Oldroyd's upper convection derivative in this model. Nawaz et al. [32] investigated the performance of shear rate-dependent viscosity fluids along a heated rotating cone using hall and ion slip currents. They explained that increasing thermal relaxation time causes the fluid temperature to fall. Gangadhar et al. [33] investigate entropy generation in the MHD flow of a Williamson nanofluid flow. Salahuddin et al. [34] investigated the Cattaneo-Christov theory for variable viscosity heat and mass fluxes. Several results from this study are discussed in these articles [35–40].

The preceding investigations expressly state that no work has been initiated to investigate Cattaneo-Christov heat motion in the progression of MHD Jeffrey liquid by the stretchable cylinder. The current work is unique in that no one has used the stagnation point flow of Jeffrey liquid in the Cattaneo model. This work is done in order to improve and be more practical. Furthermore, finite element-based simulation recognized the numerical solution's convergence and accuracy. It effectively, quickly, and precisely resolves BVP [27,32]. The current work is correlated with previously distributed information.

2. Formation

2.1. Movement analysis

Consider the EMHD flow of a nonlinear liquid along a stretching cylinder at the point of stagnation. By applying equal forces in opposite directions but with the same magnitude while holding the origin constant, the stretching velocity $\tilde{u}_w = \tilde{u}_0 \left(\frac{\tilde{x}_1}{S} \right)$ changed. In the presence of an applied magnetic-field B_0 and electric-field E_0 , the effect of stagnation is introduced

in the momentum equation. Consider cylindrical coordinates system for problem formulation. Jeffery fluid is taken along the \tilde{x}_1 -axis, and fluid deformation is taken along the radial axis.

Under the influence of the stagnation point, diffusion of fluid molecules during deformation is shown by the momentum equation. After boundary layer approximations, the flow problems are [1,41]

$$\frac{\partial(\tilde{r}_1 \tilde{u}_1)}{\partial \tilde{x}_1} + \frac{\partial(\tilde{r}_1 \tilde{v}_1)}{\partial \tilde{r}_1} = 0, \quad (1)$$

$$\begin{aligned} \tilde{u}_1 \frac{\partial \tilde{u}_1}{\partial \tilde{x}_1} + \tilde{v}_1 \frac{\partial \tilde{u}_1}{\partial \tilde{r}_1} = U_e(\tilde{x}_1) \frac{dU_e(\tilde{x}_1)}{d\tilde{x}_1} + \frac{\sigma_1}{\rho_1} (E_0 B_0 - B_0^2) (\tilde{u}_1 - U_e(\tilde{x}_1)) \\ + \frac{\mu}{\rho_1(1 + \lambda_1)} \left\{ \frac{1}{\tilde{r}_1} \frac{\partial \tilde{u}_1}{\partial \tilde{r}_1} + \frac{\partial^2 \tilde{u}_1}{\partial \tilde{r}_1^2} + \lambda_2 \left(\begin{aligned} & \frac{\tilde{v}_1}{\tilde{r}_1} \frac{\partial^2 \tilde{u}_1}{\partial \tilde{r}_1^2} + \frac{\partial \tilde{v}_1}{\partial \tilde{x}_1} \frac{\partial^2 \tilde{u}_1}{\partial \tilde{r}_1^2} + \tilde{v}_1 \frac{\partial^3 \tilde{u}_1}{\partial \tilde{r}_1^3} \\ & + \frac{\tilde{u}_1}{\tilde{r}_1} \frac{\partial^2 \tilde{u}_1}{\partial \tilde{x}_1 \partial \tilde{r}_1} + \frac{\partial \tilde{u}_1}{\partial \tilde{r}_1} \frac{\partial^2 \tilde{u}_1}{\partial \tilde{r}_1 \partial \tilde{x}_1} + \tilde{u}_1 \frac{\partial^3 \tilde{u}_1}{\partial \tilde{x}_1 \partial \tilde{r}_1^2} \end{aligned} \right) \right\}, \quad (2) \end{aligned}$$

With

$$\tilde{u}_1 = \tilde{u}_w \left(\frac{U_0}{s} \right) \tilde{x}_1, \quad \tilde{v}_1 = 0, \quad \text{at } \tilde{r}_1 = b, \quad (3)$$

$$\tilde{u}_1 \rightarrow U_e(\tilde{x}_1) = \frac{U_\infty \tilde{x}_1}{s}, \quad \text{at } \tilde{r}_1 \rightarrow \infty, \quad (4)$$

where $(\tilde{u}_1, \tilde{v}_1)$ are the velocities in $(\tilde{x}_1, \tilde{r}_1)$ -directions, \tilde{u}_w is the stretching velocity, U_∞ is the velocity of free stream, U_0 is the reference velocity, b is the radius, ρ_1 is the density, σ_1 is the electrical conductivity, μ is the kinetic viscosity, s is the characteristic length, λ_1 is the relaxation time, and λ_2 is the retardation time.

2.2. Study of energy

Fourier's law with constant thermal conductivity demonstrates the characteristics of heat transport methods (modified version). Furthermore, heat transport properties are simulated to see how they are affected by thermal radiations. Furthermore, the effect of the heat source on the study of heat transfer is observed. The impact of Cattaneo heat flux is taken into account in the energy equation. T_w is the fluid's wall temperature. Similarly, at the boundary, T_∞ is the temperature. Thus, after boundary layer approximations [34], the energy equation is

$$\rho_1 C_p \left(\tilde{u}_1 \frac{\partial T}{\partial \tilde{x}_1} + \tilde{v}_1 \frac{\partial T}{\partial \tilde{r}_1} \right) = -\nabla \cdot \vec{q}_1 + Q_0(T - T_\infty) - \frac{\partial q_{rad}}{\partial \tilde{r}_1}, \quad (5)$$

In the above equation, C_p represents specific heat, Q_0 is the heat source, and heat flux \vec{q}_1 satisfies the given below

$$\vec{q}_1 + \lambda_3 \left(\frac{\partial \vec{q}_1}{\partial t} + (\nabla \cdot V) \vec{q}_1 + V \cdot \nabla \vec{q}_1 - \vec{q}_1 \cdot \nabla V \right) = -\kappa \nabla T, \quad (6)$$

Here, λ_3 is the heat flux relaxation time. When $\lambda_3 = 0$, Fourier's law is satisfied by Equation (6); $\nabla \cdot V = 0$ (an incompressible fluid is considered). Equation (6) takes the

following form:

$$\bar{q}_1 + \lambda_3 \left(\frac{\partial \bar{q}_1}{\partial t} + V \cdot \nabla \bar{q}_1 - \bar{q}_1 \cdot \nabla V \right) = -\kappa \nabla T, \quad (7)$$

By using Roseland diffusion approximation, radiative heat flux q_{rad} is [24]:

$$q_{rad} = -\frac{4\sigma^* \partial T^4}{3k^* \partial \tilde{r}_1} = -\frac{16\sigma^* T_\infty^3 \partial T}{3k^* \partial \tilde{r}_1} \quad (8)$$

Then, Equation (5) becomes

$$\begin{aligned} & \tilde{u}_1 \frac{\partial T}{\partial \tilde{x}_1} + \tilde{v}_1 \frac{\partial T}{\partial \tilde{r}_1} + \lambda_3 \left\{ \begin{aligned} & \tilde{u}_1^2 \frac{\partial^2 T}{\partial \tilde{x}_1^2} + \tilde{v}_1^2 \frac{\partial^2 T}{\partial \tilde{r}_1^2} + 2\tilde{u}_1 \tilde{v}_1 \frac{\partial^2 T}{\partial \tilde{x}_1 \partial \tilde{r}_1} \\ & + \tilde{u}_1 \frac{\partial \tilde{u}_1}{\partial \tilde{x}_1} \frac{\partial T}{\partial \tilde{x}_1} + \tilde{u}_1 \frac{\partial \tilde{v}_1}{\partial \tilde{x}_1} \frac{\partial T}{\partial \tilde{r}_1} + \tilde{v}_1 \frac{\partial \tilde{u}_1}{\partial \tilde{r}_1} \frac{\partial T}{\partial \tilde{x}_1} + \tilde{v}_1 \frac{\partial \tilde{v}_1}{\partial \tilde{r}_1} \frac{\partial T}{\partial \tilde{r}_1} \end{aligned} \right\} \\ & = \frac{\kappa}{\rho_1 C_p} \left(\frac{1}{\tilde{r}_1} \frac{\partial T}{\partial \tilde{r}_1} + \frac{\partial^2 T}{\partial \tilde{r}_1^2} \right) + \frac{Q_0}{\rho_1 C_p} (T - T_\infty) + \frac{Q_0}{\rho_1 C_p} \lambda_3 \left(\tilde{u}_1 \frac{\partial T}{\partial \tilde{x}_1} + \tilde{v}_1 \frac{\partial T}{\partial \tilde{r}_1} \right) \\ & \quad + \frac{16\sigma^* T_\infty^3 \partial^2 T}{3\rho_1 C_p k^* \partial \tilde{r}_1^2}, \quad (9) \end{aligned}$$

With boundary conditions

$$T = T_w(\tilde{x}_1) = T_0 + \frac{c\tilde{x}_1}{s} \text{ at } \tilde{r}_1 = b, \quad (10)$$

$$T = T_\infty(\tilde{x}_1) = T_0 + \frac{d\tilde{x}_1}{s}, \text{ when } \tilde{r}_1 \rightarrow \infty, \quad (11)$$

Here, T_0 is the reference temperature, and c d are the dimensional stratification constants.

2.3. Mass transfer study

The mass transport+ equation demonstrates how the concentration of fluid molecules varies as a result of chemical product stratification using the Cattaneo–Christov theory. The ambient concentration is denoted by C_∞ , whereas the surface concentration is denoted by C_w . In the concentration equation, a chemical reaction is introduced with a modified heat flux [34].

$$\rho_1 C_p \left(\tilde{u}_1 \frac{\partial C}{\partial \tilde{x}_1} + \tilde{v}_1 \frac{\partial C}{\partial \tilde{r}_1} \right) = -\nabla \vec{J}_1 + k_1^* (C - C_\infty), \quad (12)$$

where \vec{J}_1 is the mass flux and k_1^* is the reaction rate.

$$\vec{J}_1 + \lambda_4 \left(\frac{\partial \vec{J}_1}{\partial t} + (\nabla \cdot V) \vec{J}_1 + V \cdot \nabla \vec{J}_1 - \vec{J}_1 \cdot \nabla V \right) = -D \nabla C, \quad (13)$$

where λ_4 is the thermal relaxation time factor, D is the Brownian diffusion. Put $\lambda_4 = 0$, Equation (13) changes to conventional Fourier's law and forms

$$\vec{J}_1 + \lambda_4 \left(\frac{\partial \vec{J}_1}{\partial t} + V \cdot \nabla \vec{J}_1 - \vec{J}_1 \cdot \nabla V \right) = -D \nabla C, \quad (14)$$

Eliminating \bar{J}_1 form Equations (12) and (14), one has

$$\begin{aligned} & \tilde{u}_1 \frac{\partial C}{\partial \tilde{x}_1} + \tilde{v}_1 \frac{\partial C}{\partial \tilde{r}_1} + \lambda_4 \left\{ \begin{aligned} & \tilde{u}_1^2 \frac{\partial^2 C}{\partial \tilde{x}_1^2} + \tilde{v}_1^2 \frac{\partial^2 C}{\partial \tilde{r}_1^2} + 2\tilde{u}_1 \tilde{v}_1 \frac{\partial^2 C}{\partial \tilde{x}_1 \partial \tilde{r}_1} \\ & + \tilde{u}_1 \frac{\partial \tilde{u}_1}{\partial \tilde{x}_1} \frac{\partial C}{\partial \tilde{x}_1} + \tilde{u}_1 \frac{\partial \tilde{v}_1}{\partial \tilde{x}_1} \frac{\partial C}{\partial \tilde{r}_1} + \tilde{v}_1 \frac{\partial \tilde{u}_1}{\partial \tilde{r}_1} \frac{\partial C}{\partial \tilde{x}_1} + \tilde{v}_1 \frac{\partial \tilde{v}_1}{\partial \tilde{r}_1} \frac{\partial C}{\partial \tilde{r}_1} \end{aligned} \right\} \\ & = D \left(\frac{1}{\tilde{r}_1} \frac{\partial C}{\partial \tilde{r}_1} + \frac{\partial^2 C}{\partial \tilde{r}_1^2} \right) - k_1^* (C - C_\infty) - k_1^* \lambda_4 \left(\tilde{u}_1 \frac{\partial C}{\partial \tilde{x}_1} + \tilde{v}_1 \frac{\partial C}{\partial \tilde{r}_1} \right), \end{aligned} \quad (15)$$

By suitable boundary conditions

$$C = C_w(\tilde{x}_1) = C_0 + \frac{c^* \tilde{x}_1}{s} \text{ at } \tilde{r}_1 = b, \quad (16)$$

$$C = C_\infty(\tilde{x}_1) = C_0 + \frac{d^* \tilde{x}_1}{s}, \text{ when } \tilde{r}_1 \rightarrow \infty. \quad (17)$$

In the above equation, C_0 is the reference concentration, and c^* d^* are the dimensional constants.

The arrangement of the current system can be executed with the appropriately presented beginning circumstances. Be that as it may, for similar solutions, the following equations are considered.

$$\begin{aligned} \eta &= \sqrt{\frac{U_0}{us}} \left(\frac{\tilde{r}_1^2 - b^2}{2b} \right), \quad \tilde{u}_1 = \frac{\tilde{x}_1 U_0}{s} F'_1(\eta), \quad \tilde{v}_1 = -\frac{b}{\tilde{r}_1} \sqrt{\frac{U_0}{us}} F_1(\eta), \\ \theta_1(\eta) &= \frac{T - T_\infty}{T_w - T_0}, \quad \varphi_1(\eta) = \frac{C - C_\infty}{C_w - C_0}. \end{aligned} \quad (18)$$

Equation (1) is trivial yet equations (2, 9, 15) with conditions applied

$$\begin{aligned} & (1 + 2\alpha\eta)F_1''' + (1 + \lambda_1)(F_1 F_1'' - F_1'^2) + 2\alpha F_1'' + \alpha\beta(F_1' F_1'' - 3F_1 F_1''') \\ & + (1 + 2\alpha\eta)\beta(F_1'^2 - F_1 F_1''') + (1 + \lambda_1)A^2 + M(E_0 + A - F_1') = 0, \end{aligned} \quad (19)$$

$$\begin{aligned} & (1 + 2\alpha\eta) \left(1 + \frac{4}{3} Rd \right) \theta_1'' + 2\alpha\theta_1' + \text{Pr}(1 - \gamma\delta)F_1\theta_1' - \text{Pr}S(1 - \gamma\delta)F_1' \\ & - \text{Pr}(1 - \gamma\delta)F_1' \theta_1 + \text{Pr}\gamma\{(S + \theta_1)F_1 F_1'' + F_1 F_1' \theta_1' \\ & - (S + \theta_1)F_1'^2 - F_1^2 \theta_1''\} + \text{Pr}\delta\theta_1 = 0, \end{aligned} \quad (20)$$

$$\begin{aligned} & (1 + 2\alpha\eta)\varphi_1'' + 2\alpha\varphi_1' + Sc(1 + \gamma_1\delta_1)F_1\varphi_1' - ScS_1(1 + \gamma_1\delta_1)F_1' - Sc(1 + \gamma_1\delta_1)F_1'\varphi_1 \\ & + Sc\gamma_1\{(S_1 + \varphi_1)F_1 F_1'' + F_1 F_1' \varphi_1' - (S_1 + \varphi_1)F_1'^2 - F_1^2 \varphi_1''\} - Sc\delta_1\varphi_1 = 0, \end{aligned} \quad (21)$$

$$F_1(0) = 0, F_1'(0) = 1, \theta_1(0) = 1 - S, \varphi_1(0) = 1 - S_1,$$

$$F_1'(\infty) = A, \theta_1(\infty) = 0, \varphi_1(\infty) = 0, \quad (22)$$

where α is the curvature parameter, β is in the form of retardation Deborah number, A is the movements ratio, M is the magnetic field factor, E_1 is the electric factor, Rd is the radiation factor, S is the thermal stratified variable, S_1 is the solutal stratified variable, Pr is the Prandtl number, Sc is the Schmidt number, δ is the heat source factor, δ_1 is the chemical reaction

variable, γ is thermal relaxation parameter, and γ_1 is the concentration relaxation factor. These variables are defined as:

$$\begin{aligned}\alpha &= \left(\frac{vs}{U_0 b^2} \right)^{1/2}, \beta = \frac{\lambda_2 U_0}{s}, A = \frac{U_\infty}{U_0}, S = \frac{d}{c}, S_1 = \frac{d^*}{c^*}, \\ Pr &= \frac{\nu \rho_1 C_p}{\kappa}, M = \frac{\sigma_1 B_0^2}{U_0 \rho_1}, E_1 = \frac{E_0}{u_w B_0}, Rd = \frac{4\sigma^* T_\infty^3}{\kappa k^*}, \\ Sc &= \frac{\nu}{D}, \delta = \frac{s Q_0}{U_0 \rho_1 C_p}, \delta_1 = \frac{k_1^* s}{U_0}, \gamma = \frac{\lambda_3 U_0}{s}, \gamma_1 = \frac{\lambda_4 U_0}{s}.\end{aligned}\quad (23)$$

2.4. Physical quantities

In engineering perspective, the parameters like skin friction C_f , Nusselt number Nu_r and Sherwood number Sh_r calculate the shear stress, heat transport and mass transport rates at the surface are

$$\begin{aligned}C_f &= \frac{2}{\rho_1 u_w^2} \left[\frac{\mu}{1 + \lambda_1} \left(\frac{\partial \tilde{u}_1}{\partial \tilde{r}_1} \right) + \frac{\mu \lambda_2}{1 + \lambda_1} \left(\tilde{v}_1 \frac{\partial^2 \tilde{u}_1}{\partial \tilde{r}_1^2} + \tilde{u}_1 \frac{\partial^2 \tilde{u}_1}{\partial \tilde{x}_1 \partial \tilde{r}_1} \right) \right]_{\tilde{r}_1=b}, \\ Nu &= -\frac{\tilde{x}_1}{T_w - T_\infty} \left[1 + \frac{16\sigma^* T_\infty^3}{3\kappa k^*} \right] \left(\frac{\partial T}{\partial \tilde{r}_1} \right)_{\tilde{r}_1=b},\end{aligned}\quad (24)$$

Non-dimensional forms are given below:

$$\begin{aligned}\frac{C_f \sqrt{Re}}{2} &= \frac{1}{1 + \lambda_1} [F_1''(0) - \alpha \beta F_1(0) F_1''(0) - \beta F_1(0) F_1'''(0) + \beta F_1'(0) F_1''(0)], \\ \frac{Nu}{\sqrt{Re}} &= -\left(1 + \frac{4}{3} Rd \right) \theta_1'(0), \\ \frac{Sh}{\sqrt{Re}} &= -\phi_1'(0).\end{aligned}\quad (25)$$

In which $Re = \frac{u_w \tilde{x}_1}{\nu}$ is the Reynolds number.

3. Numerical technique

The transformed equations (19)–(22) are numerically solved using the FEM technique with a Galerkin weighted residual system. At the moment, this technique is very useful in engineering applications. Solving integral equations, including CFD problems, is an extremely effective technique for solving several nonlinear differential equations. First, we consider (19)–(22).

$$F_1' = p, \quad (26)$$

$$p' = q, \quad (27)$$

The set of Equations (19)–(22), thus the reduced system, is

$$a_1 q' + (1 + \lambda_1)(F_1 q - p^2) + 2\alpha q + \alpha\beta(pq - 3F_1 q') + a_1\beta(q^2 - F_1 q'') + (1 + \lambda_1)A^2 + M(E_0 + A - p) = 0, \quad (28)$$

$$a_1 b_1 \theta_1'' + 2\alpha\theta_1' + \text{Pr} F_1 \theta_1' - \text{Pr} S b_2 p - \text{Pr} b_2 p \theta_1 + \text{Pr} \gamma \{S F_1 q + \theta_1 F_1 q + F_1 p \theta_1' - S p^2 - \theta_1 p^2 - F_1^2 \theta_1''\} + \text{Pr} \delta \theta_1 = 0, \quad (29)$$

$$a_1 \phi_1'' + 2\alpha\phi_1' + S c c_1 F_1 \phi_1' - S c S_1 c_1 p - S c c_1 p \phi_1 + S c \gamma_1 S_1 F_1 q + S c \gamma_1 \phi_1 F_1 p \phi_1' - S c \gamma_1 S_1 p^2 - S c \gamma_1 \phi_1 p^2 - S c \gamma_1 F_1^2 \phi_1'' - S c \delta_1 \phi_1 = 0, \quad (30)$$

$$F_1(0) = 0, p(0) = 1, \theta_1(0) = 1 - S, \phi_1(0) = 1 - S_1, \quad (31)$$

$$p(\infty) = A, \phi_1(\infty) = 0, \theta_1(\infty) = 0. \quad (32)$$

In above equations $a_1 = 1 + 2\alpha\eta$, $b_1 = 1 + \frac{4}{3}Rd$, $b_2 = 1 - \delta\gamma$, $c_1 = 1 + \delta_1\gamma_1$. For sake of numerical computation, $\eta \rightarrow \infty$ choose η_{max} . No more difference is detected for η greater than η_{max} after various trials so for η_{max} (i.e. $\eta \rightarrow \infty$) is fixed as $\eta_{max} = 10$. The variation associated with Equations (26)–(30) along a quadratic element $\Omega_\eta = (\eta_{\bar{a}}, \eta_{\bar{a}+1})$ is given by:

$$\int_{\eta_{\bar{a}}}^{\eta_{\bar{a}+1}} \tilde{w}_1 (F_1' - p) d\eta = 0, \quad (33)$$

$$\int_{\eta_{\bar{a}}}^{\eta_{\bar{a}+1}} \tilde{w}_2 (p' - q) d\eta = 0, \quad (34)$$

$$\int_{\eta_{\bar{a}}}^{\eta_{\bar{a}+1}} \tilde{w}_3 \left(a_1 q' + (1 + \lambda_1)(F_1 q - p^2) + 2\alpha q + \alpha\beta(pq - 3F_1 q') + a_1\beta(q^2 - F_1 q'') + (1 + \lambda_1)A^2 + M(E_0 + A - p) \right) d\eta = 0, \quad (35)$$

$$\int_{\eta_{\bar{a}}}^{\eta_{\bar{a}+1}} \tilde{w}_4 \left(a_1 b_1 \theta_1'' + 2\alpha\theta_1' + \text{Pr} F_1 \theta_1' - \text{Pr} S b_2 p - \text{Pr} b_2 p \theta_1 + \text{Pr} \gamma \{S F_1 q + \theta_1 F_1 q + F_1 p \theta_1' - S p^2 - \theta_1 p^2 - F_1^2 \theta_1''\} + \text{Pr} \delta \theta_1 \right) d\eta = 0, \quad (36)$$

$$\int_{\eta_{\bar{a}}}^{\eta_{\bar{a}+1}} \tilde{w}_5 \left(a_1 \phi_1'' + 2\alpha\phi_1' + S c c_1 F_1 \phi_1' - S c S_1 c_1 p - S c c_1 p \phi_1 + S c \gamma_1 S_1 F_1 q + S c \gamma_1 \phi_1 F_1 p \phi_1' - S c \gamma_1 S_1 p^2 - S c \gamma_1 \phi_1 p^2 - S c \gamma_1 F_1^2 \phi_1'' - S c \delta_1 \phi_1 \right) d\eta = 0, \quad (37)$$

where arbitrary form functions are $\tilde{w}_1, \tilde{w}_2, \tilde{w}_3, \tilde{w}_4$ and \tilde{w}_5 . The FEM was obtained from Equations (33)–(37) using the below approximations:

$$\bar{F}_1 = \sum_{n=1}^3 \bar{F}_n \Psi_n, \bar{p} = \sum_{n=1}^3 \bar{p}_n \Psi_n, \bar{\theta}_1' = \sum_{n=1}^3 \bar{\theta}_n' \Psi_n, \bar{q} = \sum_{n=1}^3 \bar{q}_n \Psi_n, \bar{\phi}_1' = \sum_{n=1}^3 \bar{\phi}_n' \Psi_n, \quad (38)$$

With $\tilde{w}_1 = \tilde{w}_2 = \tilde{w}_3 = \tilde{w}_4 = \tilde{w}_5 = \Psi_n$ ($n = 1, 2, 3$), where test functions Ψ_n for a typical length element $\Omega_e = (\eta_{\bar{a}}, \eta_{\bar{a}+1})$ are given by

$$\begin{aligned} \Psi_1 &= \frac{(\eta_{\bar{a}+1} - \eta_{\bar{a}} - 2\eta)(\eta_{\bar{a}+1} - \eta)}{(\eta_{\bar{a}+1} - \eta_{\bar{a}})^2}, \\ \Psi_2 &= \frac{4(\eta - \eta_{\bar{a}})(\eta_{\bar{a}+1} - \eta)}{(\eta_{\bar{a}+1} - \eta_{\bar{a}})^2}, \\ \Psi_3 &= -\frac{(\eta_{\bar{a}+1} - \eta_{\bar{a}} - 2\eta)(\eta - \eta_{\bar{a}})}{(\eta_{\bar{a}+1} - \eta_{\bar{a}})^2}, \eta_{\bar{a}} \leq \eta \leq \eta_{\bar{a}+1}. \end{aligned} \quad (39)$$

The developed equation is

$$\begin{bmatrix} [M^{11}] & [M^{12}] & [M^{13}] & [M^{14}] & [M^{15}] \\ [M^{21}] & [M^{22}] & [M^{23}] & [M^{24}] & [M^{25}] \\ [M^{31}] & [M^{32}] & [M^{33}] & [M^{34}] & [M^{35}] \\ [M^{41}] & [M^{42}] & [M^{43}] & [M^{44}] & [M^{45}] \\ [M^{51}] & [M^{52}] & [M^{53}] & [M^{54}] & [M^{55}] \end{bmatrix} \begin{bmatrix} \{F\} \\ \{p\} \\ \{q\} \\ \{\theta\} \\ \{\phi\} \end{bmatrix} = \begin{bmatrix} \{b_1\} \\ \{b_2\} \\ \{b_3\} \\ \{b_4\} \\ \{b_5\} \end{bmatrix}, \quad (40)$$

where $[M_{mn}]$ and $[b_m]$ ($m, n = 1, 2, 3, 4, 5$) are defined as:

$$M^{11} = \int_{\eta_{\bar{a}}}^{\eta_{\bar{a}+1}} \Psi_i \frac{d\Psi_j}{d\eta} d\eta, M^{12} = - \int_{\eta_{\bar{a}}}^{\eta_{\bar{a}+1}} \Psi_i \Psi_j d\eta, M^{13} = M^{14} = M^{15} = 0, b_1 = 0,$$

$$M^{21} = 0, M^{22} = \int_{\eta_{\bar{a}}}^{\eta_{\bar{a}+1}} \Psi_i \frac{d\Psi_j}{d\eta} d\eta, M^{23} = - \int_{\eta_{\bar{a}}}^{\eta_{\bar{a}+1}} \Psi_i \Psi_j d\eta, M^{24} = M^{25} = 0, b_2 = 0,$$

$$M^{31} = 0, M^{32} = \int_{\eta_{\bar{a}}}^{\eta_{\bar{a}+1}} (\alpha\beta\bar{q} - M - (1 + \lambda_1)\bar{p}) \Psi_i \Psi_j d\eta, M^{34} = M^{35} = 0,$$

$$M^{33} = \int_{\eta_{\bar{a}}}^{\eta_{\bar{a}+1}} \left[\{(1 + \lambda_1)\bar{F}_1 + 2\alpha + a_1\beta\bar{q}\} \Psi_i \Psi_j + (a_1 - 3\alpha\beta\bar{F}_1) \Psi_i \frac{d\Psi_j}{d\eta} + a_1\beta\bar{F}_1 \frac{d\Psi_i}{d\eta} \frac{d\Psi_j}{d\eta} \right] d\eta,$$

$$b_3 = a_1\beta\bar{F}_1 \left(\Psi_i \frac{dq}{d\eta} \right)_{\eta_{\bar{a}}}^{\eta_{\bar{a}+1}} - [(1 + \lambda_1)A^2 + M(E_0 + A)] \int_{\eta_{\bar{a}}}^{\eta_{\bar{a}+1}} \Psi_i d\eta,$$

$$M^{41} = 0, M^{42} = \int_{\eta_{\bar{a}}}^{\eta_{\bar{a}+1}} (-PrSb_2 - Pr\gamma S\bar{p}) \Psi_i \Psi_j d\eta, M^{43} = \int_{\eta_{\bar{a}}}^{\eta_{\bar{a}+1}} (Pr\gamma S\bar{F}_1) \Psi_i \Psi_j d\eta, M^{45} = 0,$$

$$M^{44} = \int_{\eta_{\bar{a}}}^{\eta_{\bar{a}+1}} \left[(Pr\gamma\bar{F}_1\bar{q} - Pr\gamma\bar{p}^2 + Pr\delta) \Psi_i \Psi_j + (2\alpha + Pr\bar{F}_1 - Prb_2\bar{p} + Pr\gamma\bar{F}_1\bar{p}) \Psi_i \frac{d\Psi_j}{d\eta} \right. \\ \left. + (Pr\gamma\bar{F}_1^2 - a_1b_1) \frac{d\Psi_i}{d\eta} \frac{d\Psi_j}{d\eta} \right] d\eta,$$

$$b_4 = Pr\gamma\bar{F}_1^2 \left(\Psi_i \frac{d\theta_1}{d\eta} \right)_{\eta_{\bar{a}}}^{\eta_{\bar{a}+1}} - a_1b_1 \left(\Psi_i \frac{d\theta_1}{d\eta} \right)_{\eta_{\bar{a}}}^{\eta_{\bar{a}+1}},$$

$$M^{51} = 0, M^{52} = \int_{\eta_{\bar{a}}}^{\eta_{\bar{a}+1}} (-ScS_1c_1 - Sc\gamma_1S_1\bar{p}) \Psi_i \Psi_j d\eta, M^{53} = \int_{\eta_{\bar{a}}}^{\eta_{\bar{a}+1}} (Sc\gamma_1S_1\bar{F}_1) \Psi_i \Psi_j d\eta, M^{54} = 0,$$

$$M^{55} = \int_{\eta_{\bar{a}}}^{\eta_{\bar{a}+1}} \left[(Sc\gamma_1\bar{F}_1\bar{q} - Sc\gamma_1\bar{p}^2 - Sc\delta_1) \Psi_i \Psi_j \right. \\ \left. + (2\alpha + Sc_1\bar{F}_1 - Sc_1\bar{p} + Sc\gamma_1\bar{F}_1\bar{p}) \Psi_i \frac{d\Psi_j}{d\eta} \right. \\ \left. + (Sc\gamma_1\bar{F}_1^2 - a_1) \frac{d\Psi_i}{d\eta} \frac{d\Psi_j}{d\eta} \right] d\eta,$$

$$b_5 = a_1 \left(\Psi_i \frac{d\phi_1}{d\eta} \right)_{\eta_{\bar{a}}}^{\eta_{\bar{a}+1}} - Sc\gamma_1\bar{F}_1^2 \left(\Psi_i \frac{d\theta_1}{d\eta} \right)_{\eta_{\bar{a}}}^{\eta_{\bar{a}+1}},$$

Since no further variation is observed after increasing the number of elements (n) 660 and 360,500, the flow field is divided into 500 quadratic parts of equal size (Table 1). We can

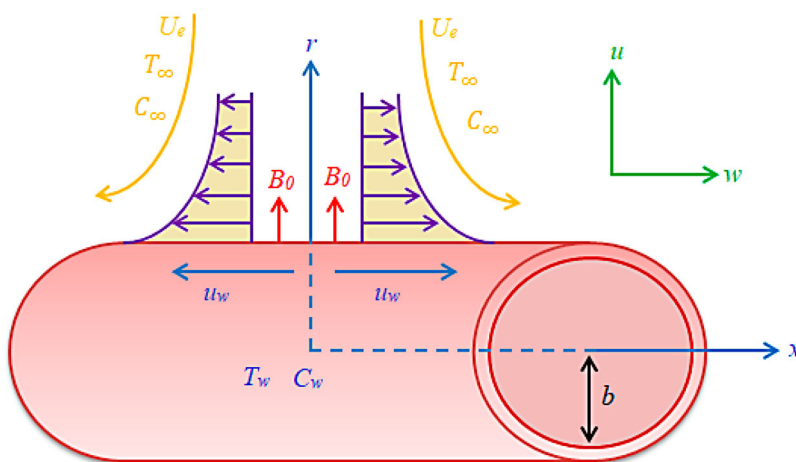


Figure 1. Physical Diagram.

Table 1. Convergence outcomes of $-f''(0)$, $-\theta_1'$ and $-\phi_1'$.

n	$-f''(0)$	$-\theta_1'$	$-\phi_1'$
20	0.678642	0.884948	0.894888
80	0.675797	0.881205	0.892714
180	0.674213	0.879069	0.891881
240	0.673227	0.877981	0.891754
360	0.672553	0.877617	0.892007
500	0.672553	0.877617	0.892007
600	0.672553	0.877617	0.892007

estimate three functions of order 2505×2505 are obtained after assembling all particle equations. The resultant matrix is nonlinear after applying boundary conditions (Equations 31–32), which is solved using the N–R technique with the required precision of 0.00005. The Gauss elimination method is used to solve a system of linear equations (see Figure 1).

4. Validation of results

Relationships with previously existing outcomes are shown in restricting cases to demonstrate the validity of the obtained mathematical results. The results of $F_1''(0)$ for values of the (ratio of moments) with other parameters are absent and parade notable agreement with published data (Table 2). Moreover, to evaluate the exactness of FEM, an association of $-\theta_1'(0)$ (Nusselt number) is also executed with published work for values of A and Pr other parameters kept as absent. Here, we noticed an excellent correlation (Table 3).

5. Results discussion

This section gives the information on vital parameters impact in flow field, heat and mass transport distribution via physical description and results from the numerical simulations. By applying finite element method all the simulations are performed. The present work is done by keeping the below values for complex parameters: $\alpha = 0.4$, $\lambda_1 = 0.2$, $\beta = 0.2$, $A =$

Table 2. Comparison of present outcomes with previous outcomes of $F_1''(0)$ for distinct values of A .

A	Mahapatra and Gupta [10]	Pop et al. [11]	Hussain et al. [1]	Present outcomes
0.1	-0.9694	-0.9694	-0.96725	-0.969386
0.2	-0.9181	-0.9181	-0.91529	-0.918107
0.5	-0.6673	-0.6673	-0.66838	-0.667264
2	2.0175	2.0174	-	2.017503
3	4.7293	4.729	-	4.729282

Table 3. Comparison of present work with previous work of $-\theta_1'(0)$ for distinct values of A and Pr .

A	Mahapatra and Gupta [10]		Pop et al. [11]		Present outcomes	
	Pr		Pr		Pr	
	0.5	1.5	0.5	1.5	0.5	1.5
0.1	0.383	0.777	0.381	0.773	0.382366	0.776801
0.2	0.408	0.797	0.406	0.793	0.407292	0.797122
0.5	0.473	0.863	0.471	0.859	0.472798	0.864794
1	0.563	0.974	0.562	0.97	0.56419	0.977205
2	0.709	1.171	0.708	1.168	0.711868	1.178099
3	0.829	1.341	0.828	1.339	0.833562	1.351944

$0.2, M = 0.2, E_1 = 0.1, Rd = 0.1, Pr = 0.71, \gamma = 0.1, \delta = 0.2, S = 0.1, Sc = 0.22, \gamma_1 = 0.4, \delta_1 = 0.2$ and $S_1 = 0.1$.

First, we discuss the physical interpretation of all involved parameters. Figure 2 gives the effect of magnetic parameter M and electric field factor E_1 against flow velocity. It is observed that electric and magnetic fields behave quite opposite in velocity distribution. If we increase E_1 values we observe that the flow rate is increased significantly. Physically, the Lorentz force acts as an increasing force, decreasing fluid friction by shifting the streamlines away from the cylinder surface. Furthermore, increasing the magnetic parameter M results in a significant decrease in the Jeffrey fluid flow pattern. In fact, as the influence of the magnetic parameter increases, a large amount of drag force is produced, which opposes liquid movement, and as a result, the velocity of the fluid decreases. $M \neq 0$ is associated with hydro-magnetic flow and $M = 0$ with hydro-dynamic flow pattern. We investigate the range of M between 0 and 2, as well as the range of E_1 between 0 and 0.4.

To reveal the fluid velocity behaviors of the Jeffrey liquid in relation to the curvature parameter and Deborah number over relaxation time λ_1 , as shown in Figure 3, this figure calculates the streamlines if the liquid becomes larger for a high curvature parameter. When the curvature factor is increased, the cylinder radius decreases, and the flow geometry limits the fluid interaction region. Finally, it calculates the fluid velocity and the associated boundary layer thickness. It is discovered that the radius of the cylinder can be chosen between 0.0 and 1.6. Furthermore, as λ_1 increases, the velocity and associated boundary layer exhibit a decreasing nature. It is due to the fact that a larger λ_1 , causes a longer relaxation time, which increases the resistive force for the liquid stream, and as a result, the velocity decreases. For the current study, we discovered that the scope of λ_1 can be taken between 0.0 and 2.0.

Figure 4 depicts the stimulus of Deborah number and stagnation variable A against flow curves of Jeffrey fluid. As we increased the β values, we noticed that the streamlines and thickness of the velocity boundary layer decreased, as did the retardation time, which

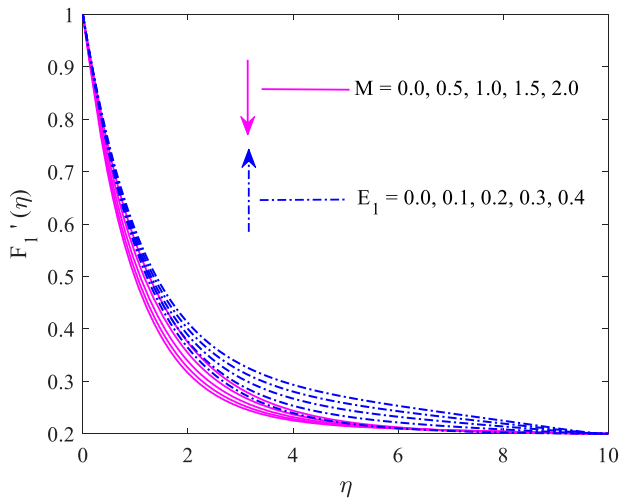


Figure 2. Velocity F_1' versus M and E_1 .

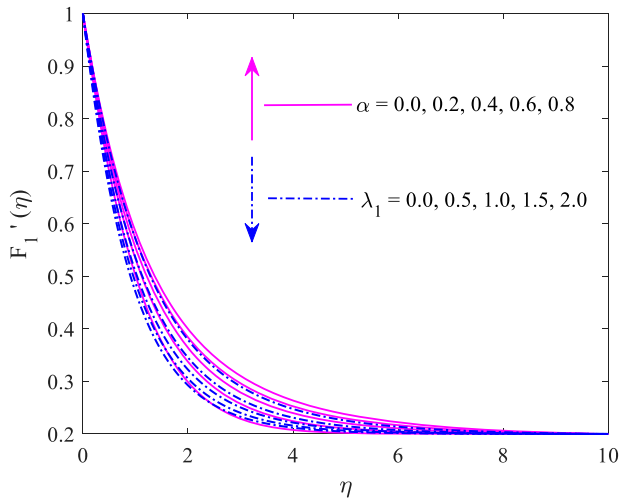


Figure 3. Velocity F_1' versus α and λ_1 .

decreased the flow field for fixed $A = 0.1$. The value of β is assumed to be between 0.0 and 8.0. Figure 4 shows that increasing A values increase the associated boundary layer thickness and velocity. With decreasing A values, the extending speed exceeds the free stream speed. As a result, the liquid stream expands. The results converge when the range of A is assumed to be between 0.15 and 0.35.

Figure 5 depicts the stimulus of curvature parameter and thermal relaxation variable on thermal curvatures. This figure demonstrates that thermal boundary layer conditions are asymptotically fulfilled, and an increase in thermal curves of Jeffrey liquid is observed as curvature parameter values are increased. Furthermore, the temperature field and its thermal boundary layer decrease, which promotes the thermal relaxation time factor. This figure clearly shows that there is a reverse connection between γ and θ_1 . This can be physically

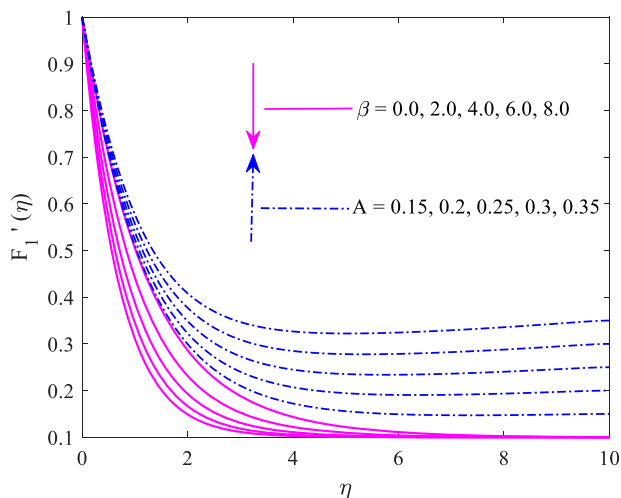


Figure 4. Velocity F_1' versus β and A .

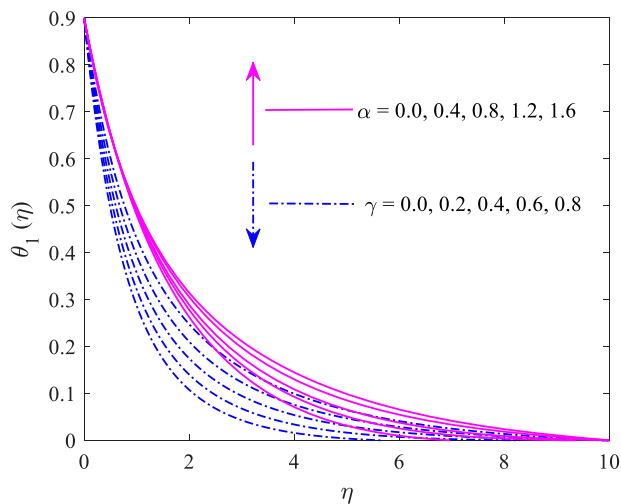


Figure 5. Temperature θ_1 versus α and γ .

depicted as an increase in the amount of time required to move heat from one molecule to another, simply putting the conduct of a non-conducting material that is liable to reduce heat transfer. We noticed that the range of γ can be taken between 0.0 and 0.8.

The temperature field for the difference in thermal stratification variable S and heat source factor is shown in Figure 6. A larger S causes the thickness of the thermal layer to decrease. It implies that the greater the S , the greater the difference between encompassing and surface temperatures. As a result, the temperature field shrinks as S increases. Subsequently, the temperature field diminishes by means of bigger S . The range of S is $0.0 \leq S \leq 0.4$. Moreover, from this figure, it is explored that the thermal curves of Jeffrey fluid portray 'increasing pattern for heat source parameter ($\delta > 0$) while depicting decreasing behavior for heat sink constraint ($\delta < 0$). Its explanation is straightforward, i.e. when the

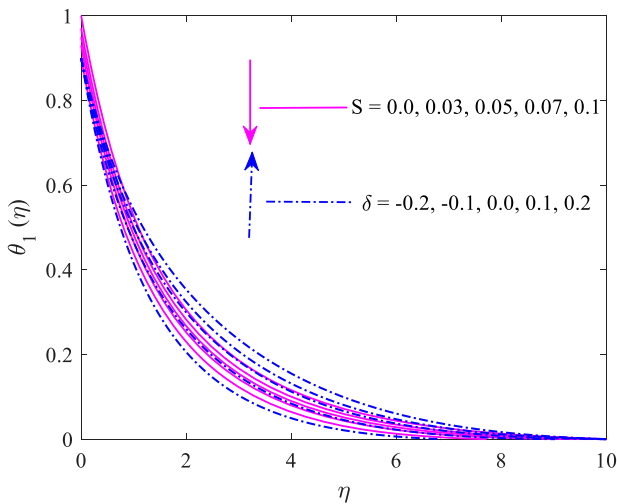


Figure 6. Temperature θ_1 versus S and δ .

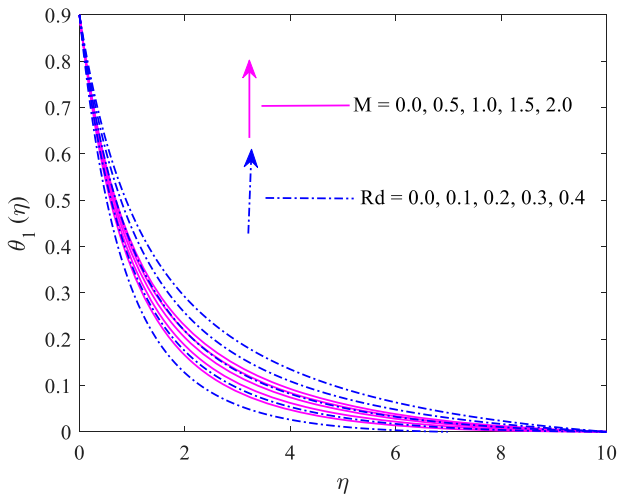


Figure 7. Temperature θ_1 versus M and Rd .

impact of any source of heat is expanded in the framework, a greater amount of heat summarizes in the framework, causing thermal dispersion of the liquid to increase; however, when we increase the advantages of heat sink imperative, a greater amount of heat waves leaves the system, causing the system temperature to decrease. For the current work, we see that the scope of the heat source is somewhere between 0.3 and 0.5.

Figure 7 depicts the temperature properties of Jeffrey fluid in the presence of the magnetic force factor M and the radiation factor Rd . For high magnetic parameter values, it is assumed that thermal energy transport in Jeffrey fluid flow decreases. In essence, a high magnetic parameter causes the Lorentz force to be strengthened, and this force causes the thermal profile of the fluid to be increased. Furthermore, as the value of Rd increases, the thickness of the thermal layer increases. The presence of radiative flux indicates that the

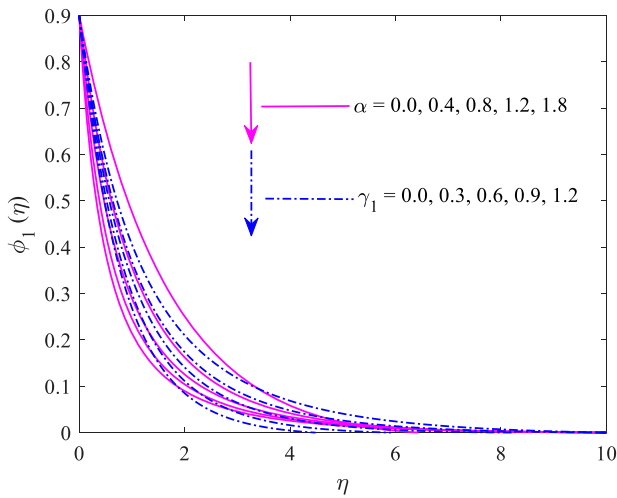


Figure 8. Concentration ϕ_1 versus α and γ_1 .

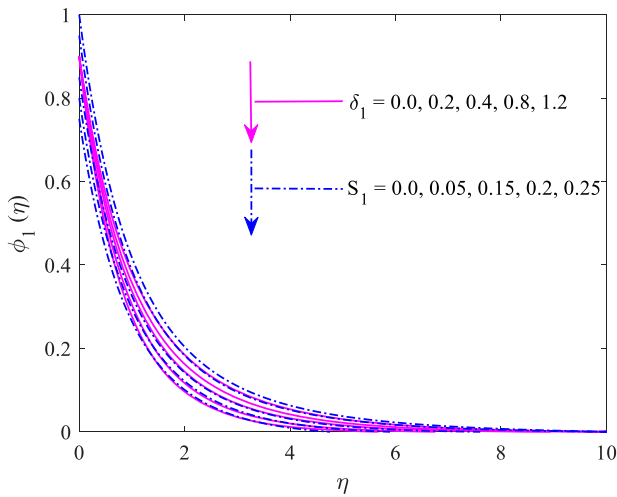


Figure 9. Concentration ϕ_1 versus δ_1 and S_1 .

liquid is preoccupied with extra heat, and thus is responsible for high temperature. The radiation factor is set to be between 0.0 and 0.4.

The influence of curvature parameter α and solutal relaxation time γ_1 on concentration curves is depicted in Figure 8. The concentration distribution decays although the thickness of the boundary layer reduces for greater α . Actually, it displays that the greater curvature variable corresponds to diminish the resistive force, and hence, the thickness of the boundary layer declines. Additionally, increasing the relaxation time reduces concentration. In the Cattaneo-Christov heat transition model, higher upswings of the relaxation time boundary physically control the moment proliferation of heat waves in a given medium. As a result of the longer relaxation time boundaries, the liquid required more space for heat and mass transfer, causing the temperature and concentration fields to decrease.

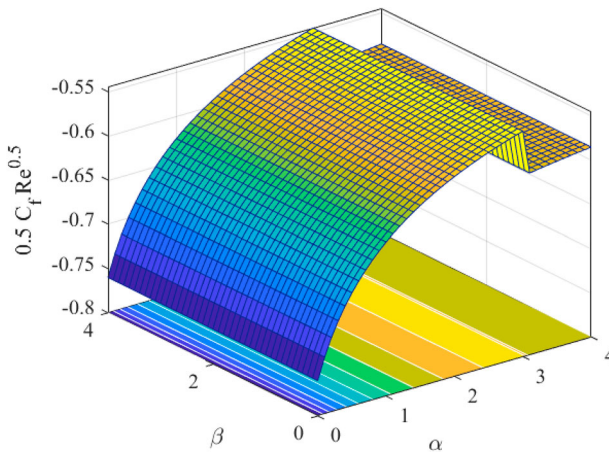


Figure 10. Skin friction versus α and β .

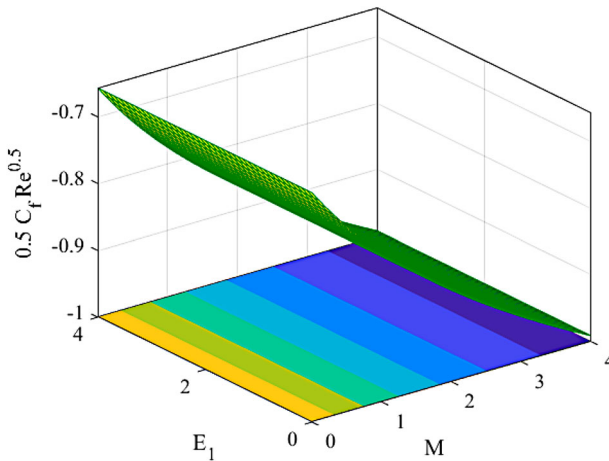


Figure 11. Skin friction versus M and E_1 .

Figure 9 discloses chemical reaction parameter δ_1 ($0.0 \leq \delta_1 \leq 1.2$) and solutal stratified variable S_1 ($0.0 \leq S_1 \leq 0.25$) on concentration. when δ_1 is increased the boundary layer thickness and the concentration field decrease. Further, the concentration field declines when S_1 increased. Physically, we detected that the variance between surface and ambient concentrations diminishes when S_1 augmented. Figure 10 presents the skin friction for different values of α and β . Coefficient of Skin friction rises for larger α and it is decreases for higher β . Applying the regression slope method through the data points, the skin friction increases at the rate 0.0331 via α while it decreases at the rate -1.01141 via β . The skin friction increases at the rate 0.102081 for E_1 , whereas declines at the rate -0.08092 due to M (see Figure 11).

Table 4 analyses the behavior of the Nusselt number for variations in certain physical parameters such as $Pr, \alpha, \gamma, \delta, S$ and A by applying the linear regression slope method over

Table 4. Nusselt number for different values of physical parameters.

Pr	α	γ	δ	S	A	$-\theta'(0)$
0.71	0.4	0.4	0.2	0.1	0.1	0.86784259
1						1.07888461
2						1.65787528
3						2.09760044
4						2.46521767
Slope						0.485221
	0.1					0.82441481
	0.5					0.88502711
	0.9					0.95480487
	1.3					1.0229101
	1.7					1.08872384
	Slope					0.166625
		0.2				0.79145167
		0.6				0.94384849
		1				1.09410775
		1.4				1.24080372
		1.8				1.38218586
		Slope				0.369606
			0.1			0.92506058
			0.3			0.80286496
			0.5			0.62953982
			0.7			0.26157189
			0.9			-0.39107351
			Slope			-1.58678
				0		0.8831258
				0.1		0.86784259
				0.2		0.85255937
				0.3		0.83727616
				0.4		0.82199294
				Slope		-0.15283
					0	0.84366071
					0.1	0.86784259
					0.2	0.89812752
					0.3	0.93165263
					0.4	0.96639681
					Slope	0.309282

the data points. The numerical values of the rate of heat transfer are shown to increase gradually with Prandtl number Pr , curvature factor α , thermal relaxation indicative parameter γ , and stagnation factor A at rates of 0.485221, 0.166625, 0.369606, and 0.309282, respectively. The heat source parameter δ , on the other hand, decreases the Nusselt number at a rate of -1.58678 , as does the parameter for the thermal stratified medium S .

Table 5 displays the slope regression analysis of local Sherwood number for the data points of the physical parameters Sc , α , γ_1 , δ_1 , S_1 and M . The mass transfer rate increases at the rate 1.018851, 0.845908, 0.245643 and 0.227276 via Sc , α , γ_1 and δ_1 correspondingly, however, the mass transfer rate decreases at the rate of -0.55862 and -0.02108 via S_1 and M .

6. Conclusion

We investigated a steady motion of Jeffrey liquid over a stretching cylinder in a stagnation point flow in this paper. In this study, the significant features of the electric field and the Cattaneo-Christov heat flux model with double stratification are investigated. Using the

Table 5. Sherwood number for different values of physical parameters.

Sc	α	γ_1	δ_1	S_1	M	$-\phi'(0)$
0.22	0.4	0.4	0.2	0.1	0.2	0.88713444
0.62						1.39284997
0.78						1.54983503
0.82						1.58661156
1.25						1.93749829
Slope						1.018851
	0.1					0.63519995
	0.5					0.97094398
	0.9					1.30754569
	1.3					1.64695627
	1.7					1.98901069
	Slope					0.845908
		0.2				0.83396331
		0.6				0.93912853
		1				1.03961896
		1.4				1.13553711
		1.8				1.22704482
		Slope				0.245643
			0.1			0.86088824
			0.3			0.91212211
			0.5			0.95895337
			0.7			1.00236847
			0.9			1.04304108
			Slope			0.227276
				0		0.94299665
				0.1		0.88713444
				0.2		0.83127223
				0.3		0.77541003
				0.4		0.71954782
				Slope		-0.55862
					0.1	0.89013879
					0.5	0.8790978
					0.9	0.87014371
					1.3	0.86264538
					1.7	0.85621248
					Slope	-0.02108

finite element method (FEM) on ODEs, the physical outputs are revealed. The main findings are summarized as follows:

1. For heat source ($\delta > 0$) parameter the temperature dispersion of Jeffrey fluid accelerated though inverse nature is noted for sink constraint ($\delta < 0$).
2. The reduction performance of the thermal field and the thickness of the thermal layer of the Jeffrey magnetic fluid are revealed as the thermal relaxation factor and thermal stratified parameter values increase.
3. For improving values of the magnetic parameter, curvature factor, and radiation parameter, the temperature distribution of the Jeffrey liquid accelerates.
4. For curvature parameter, solutal relaxation time, and chemical reaction rate constraint, the concentration curves of electrical Jeffrey liquid decrease.
5. The wall heat transport rate decreases as the heat source factor and thermal stratification parameter increases, while increasing the values of the curvature parameter, Prandtl number, and thermal relaxation time constraint.

- The Sherwood number increases as the Schmidt number and Solutal relaxation time increase, but decreases as the magnetic indicative parameter increases.

The current work results may be useful in industries such as electronic cooling and heat exchangers by controlling the rate of heat transfer. In this case, thermal relaxation time with Oldroyd upper convective derivative is usually expert variable t is used to control and examine the particular t time for heat flux from the heated region. Our further research will examine Cattaneo–Christov model for Jeffrey nanofluid under the influence of nonlinear radiations.

Acknowledgements

The authors are highly obliged and thankful to unanimous reviewers for their valuable comments on the paper.

Disclosure statement

No potential conflict of interest was reported by the author's.

References

- Hussain Z, Hussain A, Anwar MS, et al. Analysis of Cattaneo–Christov heat flux in Jeffrey fluid flow with heat source over a stretching cylinder. *J Therm Anal Calorim.* 2022;147:3391–3402.
- Ijaz Khan M, Alzahrani F. Nonlinear dissipative slip flow of Jeffrey nanomaterial towards a curved surface with entropy generation and activation energy. *Math Comput Simul.* 2021;185:47–61.
- Bhatti MM, Jun S, Khalique CM, et al. Lie group analysis and robust computational approach to examine mass transport process using Jeffrey fluid model. *Appl Math Comput.* 2022;421:126936.
- Peshkov I, Dumbser M, Boscheri W, et al. Simulations of non-Newtonian viscoplastic flows with a unified first order hyperbolic model and a structure-preserving semi-implicit scheme. *Comput Fluids.* 2021;224:104963.
- Ketchate CGN, Kapen PT, Fokwa D, et al. Stability analysis of non-Newtonian blood flow conveying hybrid magnetic nanoparticles as target drug delivery in presence of inclined magnetic field and thermal radiation: application of therapy of cancer. *Inform Med Unlocked.* 2021;27:100800.
- Selimefendigil F, Oztop HF. Thermal management for conjugate heat transfer of curved solid conductive panel coupled with different cooling systems using non-Newtonian power law nanofluid applicable to photovoltaic panel systems. *Int J Therm Sci.* 2022;173:107390.
- Loenko DS, Shenoy A, Sheremet MA. Effect of time-dependent wall temperature on natural convection of a non-Newtonian fluid in an enclosure. *Int J Therm Sci.* 2021;166:106973.
- Nadeem S, Akhtar S, Saleem A. Peristaltic flow of a heated Jeffrey fluid inside an elliptic duct: streamline analysis. *Appl Math Mech-Engl Ed.* 2021;42:583–592.
- Oke AS. Theoretical analysis of modified Eyring Powell fluid flow. *J Taiw Inst Chem Eng.* 2022;132:104152.
- Mahapatra TR, Gupta AS. Heat transfer in stagnation-point flow towards a stretching sheet. *Heat Mass Transfer.* 2002;38:517–521.
- Pop SR, Grosan T, Pop I. Radiation effects on the flow near the stagnation point of a stretching sheet. *Techn Mech.* 2004;25:100–106.
- Mandal PK, Seth GS, Sarkar S, et al. A numerical simulation of mixed convective and arbitrary oblique radiative stagnation point slip flow of a CNT-water MHD nanofluid. *J Therm Anal Calorim.* 2021;143:1901–1916.
- Iqbal Z, Khan M, Ahmed A. On modified Fourier heat flux in stagnation point flow of magnetized Burgers' fluid subject to homogeneous-heterogeneous reactions. *J Therm Anal Calorim.* 2022;147:815–826.

- [14] Gangadhar K, Edukondala Nayak R, Venkata Subba Rao M, et al. Nodal/saddle stagnation point slip flow of an aqueous convectonal magnesium oxide-gold hybrid nanofluid with viscous dissipation. *Arab J Sci Eng.* 2021;46:2701–2710.
- [15] Shafiq A, Mebarek-Oudina F, Sindhu TN, et al. A study of dual stratification on stagnation point Walters' B nanofluid flow via radiative Riga plate: a statistical approach. *Eur Phys J Plus.* 2021;136:407.
- [16] Chu Y, Khan MI, Rehman MIU, et al. Stability analysis and modeling for the three-dimensional Darcy-Forchheimer stagnation point nanofluid flow towards a moving surface. *Appl Math Mech-Engl Ed.* 2021;42:357–370.
- [17] Zhao T, Khan MR, Chu Y, et al. Entropy generation approach with heat and mass transfer in magnetohydrodynamic stagnation point flow of a tangent hyperbolic nanofluid. *Appl Math Mech-Engl Ed.* 2021;42:1205–1218.
- [18] Nguyen MN, Sajjad T, Le RH, et al. Modified Chebyshev wavelets approach for mixed convection flow due to oblique stagnation point along a vertically moving surface with zero mass flux of nanoparticles. *J Mol Liq.* 2021;343:117569.
- [19] Khan U, Waini I, Ishak A, et al. Unsteady hybrid nanofluid flow over a radially permeable shrinking/stretching surface. *J Mol Liq.* 2021;331:115752.
- [20] Khan M, Ahmed J, Ali W. Thermal analysis for radiative flow of magnetized Maxwell fluid over a vertically moving rotating disk. *J Therm Anal Calorim.* 2021;143:4081–4094.
- [21] Luo M, Wang C, Zhao J, et al. Characteristics of effective thermal conductivity of porous materials considering thermal radiation: A pore-level analysis. *Int J Heat Mass Transf.* 2022;188:122597.
- [22] Liu M, Chen B, Zhang D, et al. Numerical studies on effective thermal conductivities of the glass/polyimide composite materials under the conditions of conduction & radiation. *Int J Heat Mass Transf.* 2021;180:121764.
- [23] Raza A, Haq RU, Shah SS, et al. Existence of dual solution for micro-polar fluid flow with convective boundary layer in the presence of thermal radiation and suction/injection effects. *Int Commun Heat Mass Transf.* 2022;131:105785.
- [24] Mumraiz S, Ali A, Awais M, et al. Entropy generation in electrical magnetohydrodynamic flow of Al_2O_3-Cu/H_2O hybrid nanofluid with non-uniform heat flux. *J Therm Anal Calorim.* 2021;143:2135–2148.
- [25] Suganya S, Muthamilsevan M, Alhussain ZA. Activation energy and Coriolis force on $Cu-TiO_2$ /water hybrid nanofluid flow in an existence of nonlinear radiation. *Appl Nanosci.* 2021;11:933–949.
- [26] Mahabaleswar US, Vishalakshi AB, Azese MN. The role of Brinkmann ratio on non-Newtonian fluid flow due to a porous shrinking/stretching sheet with heat transfer. *Eur J Mech B Fluids.* 2022;92:153–165.
- [27] Ali B, Hussain S, Abdal S, et al. Impact of Stefan blowing on thermal radiation and Cattaneo-Christov characteristics for nanofluid flow containing microorganisms with ablation/accretion of leading edge: FEM approach. *Eur Phys J Plus.* 2020;135:821.
- [28] Jamaludin A, Nazar R, Pop I. Mixed convection stagnation-point flow of cross fluid over a shrinking sheet with suction and thermal radiation. *Phys A: Stat Mech Appl.* 2022;585:126398.
- [29] Acharya N. On the flow patterns and thermal control of radiative natural convective hybrid nanofluid flow inside a square enclosure having various shaped multiple heated obstacles. *Eur Phys J Plus.* 2021;136:889.
- [30] Mahabaleswar US, Vishalakshi AB, Andersson HI. Hybrid nanofluid flow past a stretching/shrinking sheet with thermal radiation and mass transpiration. *Chin J Phys.* 2022;75:152–168.
- [31] Gangadhar K, Naga Bhargavi D, Venkata Subba Rao M, et al. Entropy minimization on magnetized Boussinesq couple stress fluid with non-uniform heat generation. *Phys Scr.* 2021;96:095205.
- [32] Nawaz M, Batool S, Elmasry Y. Influence of hybrid nano-structures on thermal performance of shear rate dependent viscosity fluid over a heated rotating cone with Hall and slip currents. *J Therm Anal Calorim.* 2022;147:697–710.
- [33] Gangadhar K, Seshakumari PM, Venkata Subba Rao M, et al. MHD flow analysis of a Williamson nanofluid due to Thomson and Troian slip condition. *Int J Appl Comput Math.* 2022;8:6.

- [34] Salahyddin T, Awais M, Khan M, et al. Analysis of transport phenomenon in cross fluid using Cattaneo-Christov theory for heat and mass fluxes with variable viscosity. *Int Commun Heat Mass Transf.* **2021**;129:105664.
- [35] Hafeez A, Khan M. Dlow of Oldroyd-B fluid caused by a rotating disk featuring the Cattaneo-Christov theory with heat generation/absorption. *Int Commun Heat Mass Transf.* **2021**;123:105179.
- [36] Nayak MK, Mabood F, Tlili I, et al. Entropy optimization analysis on nonlinear thermal radiative electromagnetic Darcy-Forchheimer flow of SWCNT/MWCNT nanomaterials. *Appl Nanosci.* **2021**;11:399–418.
- [37] Garia R, Rawat SK, Kumar M, et al. Hybrid nanofluid flow over two different geometries with Cattaneo-Christov heat flux model and heat generation: A model with correlation coefficient and probable error. *Chin J Phys.* **2021**;74:421–439.
- [38] Mushtaq T, Rauf A, Shehzad SA, et al. Numerical and statistical approach for Casson-Maxwell nanofluid flow with Cattaneo-Christov theory. *Appl Math Mech-Engl Ed.* **2021**;42:1063–1076.
- [39] Venkata Ramana K, Gangadhar K, Kannan T, et al. Cattaneo-Christov heat flux theory on transverse MHD Oldroyd-B liquid over nonlinear stretched flow. *J Therm Anal Calorim.* **2022**;147:2749–2759.
- [40] Farooq U, Waqas H, Imran M, et al. Numerical investigation for melting heat transport of nanofluids due to stretching surface with Cattaneo-Christov thermal model. *Alex Eng J.* **2022**;61(9):6635–6644.
- [41] Mehboob H, Maqbool K, Ullah H, et al. Computational analysis of an axisymmetric flow of Jeffrey fluid in a permeable micro channel. *Appl Math Comput.* **2022**;418:126826.